



Residual stresses in suspension plasma sprayed electrolytes in metal-supported solid oxide fuel cell half cells

A. Macwan^a, D.L. Chen^{a,*}, M. Marr^b, O. Kesler^b

^a Department of Mechanical and Industrial Engineering, Ryerson University, 350 Victoria Street, Toronto, Ontario M5B 2K3, Canada

^b Department of Mechanical and Industrial Engineering, University of Toronto, 5 King's College Road, Toronto, Ontario M5S 3G8, Canada

HIGHLIGHTS

- ▶ Yttria-stabilized zirconia (YSZ) electrolyte is made with suspension plasma spray.
- ▶ Residual stresses are evaluated via high-temperature X-ray diffractometry.
- ▶ Residual stresses in YSZ electrolyte layers are identified to be tensile in nature.
- ▶ With increasing temperature the residual stresses are observed to decrease.
- ▶ Torch power and stand-off distance have a strong effect on the residual stresses.

ARTICLE INFO

Article history:

Received 27 May 2012

Received in revised form

14 August 2012

Accepted 16 August 2012

Available online 24 August 2012

Keywords:

Residual stress

Metal-supported solid oxide fuel cell

Yttria stabilized zirconia

Electrolyte

Suspension plasma spraying

X-ray diffraction

ABSTRACT

Solid oxide fuel cells (SOFCs) efficiently convert chemical energy into electrical energy with fuel flexibility and low emissions. Plasma spraying has emerged as a fabrication technique for metal-supported SOFCs. Residual stresses in suspension plasma sprayed (SPS) yttria-stabilized zirconia (YSZ) electrolytes fabricated with various processing parameters and substrates were analyzed by X-ray diffraction. The temperature dependence of the residual stresses was also evaluated. The electrolyte residual stresses varied with both processing conditions and substrate characteristics, and ranged from 35 to 91 MPa. The change in stresses agreed well with the observed microstructural changes arising from the use of different processing conditions and substrates. The electrolytes fabricated using torch power and stand-off distance of 133 kW and 90 mm exhibited the highest residual stress due to their relatively dense microstructure with low level of vertical cracking compared to electrolytes made with the other spray conditions. As these electrolytes were heated from room temperature to 750 °C, residual stresses decreased from 91 to 39 MPa. The decrease is due to changes in Young's modulus and to thermal expansion mismatch between the layers, and possibly also due to the formation of additional micro-cracks or creep of the porous stainless steel substrate.

© 2012 Elsevier B.V. All rights reserved.

1. Introduction

Extensive efforts to develop low-cost and reliable solid oxide fuel cells (SOFCs) for power generation and transportation applications are motivated by the pressing need for improved fuel efficiency, reduced anthropogenic greenhouse gas emissions, and enhanced energy security [1–6]. Currently, high material and production costs and poor durability are key barriers to the widespread commercialization of SOFCs [3,7,8]. One potential approach to reduce material costs and improve durability is to use a metal-supported cell structure based upon relatively inexpensive stainless steels [9,10]. The inclusion of stainless steels necessitates the

use of intermediate operating temperatures (650–800 °C), but their high electrical and thermal conductivity, superior toughness and thermal shock resistance, and good workability are highly attractive attributes for SOFCs [11]. Thus, metal-supported SOFCs have recently received considerable attention [12–15].

When fabricating conventional anode-supported SOFCs, the electrolyte and electrode functional layers are typically deposited as wet ceramic powder slurries, which are then solidified by sintering at high temperatures. It is difficult to apply these wet ceramic fabrication methods to metal-supported SOFCs because the electrolyte sintering process could rapidly oxidize or densify the porous stainless steel supports. Alternatively, direct deposition fabrication methods such as plasma spraying may be better suited for the production of the functional layers in metal-supported SOFCs.

* Corresponding author. Tel.: +1 416 979 5000x6487; fax: +1 416 979 5265.
E-mail address: dchen@ryerson.ca (D.L. Chen).

In plasma spraying, feedstock powders are melted and accelerated by a plasma jet toward a substrate. Upon impact with the substrate, the molten particles flatten and solidify to form splats, which accumulate to form coating layers [16,17]. This process readily permits deposition of ceramic coatings on metallic supports without additional post-deposition heat treatment. As a rapid deposition process, plasma spraying could also reduce manufacturing costs, especially at low and intermediate volumes, compared to more time-consuming wet ceramic methods. Suspension plasma spraying (SPS) is a modification of the traditional plasma spray process in which the feedstock powders are suspended in liquid for feeding to the plasma rather than being fed as dry powders with the use of carrier gas. The suspension permits the use of smaller feedstock powders, so SPS could potentially be used to produce thinner coating layers and more refined microstructural features [18]. This study is focused on the electrolyte layer, which is made of 8 mol% yttria-stabilized zirconia (YSZ), and should be thin, dense, and gas-tight for good performance. As such, deposition of the electrolyte by SPS has been the subject of a number of studies [18,19].

One characteristic of plasma sprayed coatings is the presence of residual stresses, which originate from the large thermal gradients experienced during the deposition process. The residual stresses in plasma sprayed coatings can be sub-divided into two main contributions: quenching stress or primary stress, and thermal mismatch stress or secondary stress. The quenching stress arises as individual splats rapidly solidify and cool from a molten state to the substrate temperature, while their contraction is restricted by adhesion to the substrate. These quenching stresses are always tensile. Thermal mismatch stress develops during post-deposition cooling to room temperature due to the difference in the coefficients of thermal expansion (CTEs) between coating layers and substrate [20]. Thermal mismatch stress can be either tensile or compressive, depending on the relative values of the CTEs of the coating layers and substrate. In service, the applied stresses are superimposed on the residual stresses, which could increase or decrease the total stress, depending on the respective signs of each stress component. These stresses could increase the number and size of cracks in the electrolyte, which would reduce cell performance and could lead to catastrophic failure of the cell. Therefore, understanding the residual stresses arising from different processing conditions can provide useful insight into the mechanical integrity of the electrolyte prior to cell operation. Understanding residual stress may also provide useful insight toward modification of the spray process or cell design. For instance, the substrate temperature during spraying could be varied to alter quenching or thermal mismatch stresses, or the composition of the stainless steel support may be adjusted to change its thermal expansion behavior.

Since metal-supported SOFCs are operated in the 650–800 °C range, it is also of interest to ascertain residual stress values at these elevated temperatures in addition to at room temperature. Residual stress values at room and elevated temperatures in YSZ electrolytes in anode-supported or cathode-supported planar SOFCs fabricated by other processes have been previously reported [21–23]. However, to the authors' knowledge, no studies on the residual stresses in metal-supported planar SOFCs made by plasma spraying have been reported. The objective of the present study is, therefore, to identify the residual stresses of SPS YSZ electrolytes at room and elevated temperatures. The electrolytes were deposited on two types of substrates, one consisting of SOFC cathode layers on porous 430 stainless steel supports, and the other consisting of only the porous 430 stainless steel supports. Electrolytes made from various sets of spray parameters having a wide range of microstructural characteristics were tested to determine the effect of process conditions on residual stresses.

2. Experimental procedure

2.1. Plasma spray processing

The YSZ electrolyte coatings were deposited by SPS with an Axial III torch (Northwest Mettech Corp., North Vancouver, BC, Canada). Five different spray conditions, shown in Table 1, were selected. For all the spray conditions, an aqueous feedstock suspension of 8 mol% YSZ powder with a d_{50} of approximately 2.6 μm (Inframat Corp., Manchester, CT) was fed to the torch at a rate of 21 ml min^{-1} . The solid content of the suspension was 3 vol.% and polyethyleneimine was added as a dispersant. The suspension was injected axially into the plasma through a 0.84 mm ID syringe type injector, and 30 slpm N_2 was used as an atomizing gas. The substrates were preheated to ensure that their temperatures were at least 300 °C for the entire spray run, though depending on the spray conditions, peak substrate surface temperatures ranged from 430 to 770 °C. It was not possible to control substrate temperatures more precisely. The targeted thickness for all coatings was 50 μm , but the thickness of individual coatings ranged from 45 to 51 μm , except for the coatings fabricated using the G3 spray conditions, which had thicknesses of approximately 71 μm .

The electrolytes were deposited on two substrates. The LSM/YSZ + MG 2 substrates consisted of SOFC cathode layers on porous 430 stainless steel discs (Mott Corp., Farmington, CT) having a diameter of 25.4 mm and thickness of approximately 1.6 mm. The pore structure was designated as media grade (MG) 2, which indicates that only particles smaller than 2 μm should penetrate through the pore network if the discs were to be used as filters. The cathodes consisted of a composite of lanthanum strontium manganite (LSM) and YSZ and were previously deposited by plasma spraying, as described elsewhere [18]. The cathodes had an average thickness of approximately 40 μm . The electrolyte-cathode-support structure is often referred to as an SOFC “half cell”. An SEM image of a cross-section of a sample half cell is shown in Fig. 1. The second substrates were simply porous 430 stainless steel discs (Mott Corp.) having a relatively fine MG 0.2 pore structure.

2.2. X-ray diffraction measurements

Residual stresses in the electrolytes were measured using X-ray diffraction (XRD). The residual stresses in electrolytes made with all 5 spray conditions on both substrates were measured at room temperature. Residual stresses in an electrolyte made with the G2 spray condition, which had a torch power of 133 kW and a stand-off

Table 1
Suspension plasma spray parameters used to deposit the YSZ electrolyte layers.

Identifier	G1	G2 ^a	G3	G4	G5
Torch power, kW	133	133	133	100	162
Stand-off distance, mm	70	90	120	90	90
Plasma gas flow rate, slpm	275	275	275	275	275
Ar (%)	30	30	30	74	25
N ₂ (%)	65	65	65	21	70
H ₂ (%)	5	5	5	5	5
Current, A	600	600	600	600	750
Nozzle, mm	9.5 (3/8")	9.5 (3/8")	9.5 (3/8")	9.5 (3/8")	9.5 (3/8")
Substrate	LSM/YSZ + MG 2/MG 0.2				

^a Indicates the condition used to fabricate the electrolytes tested at elevated temperatures.

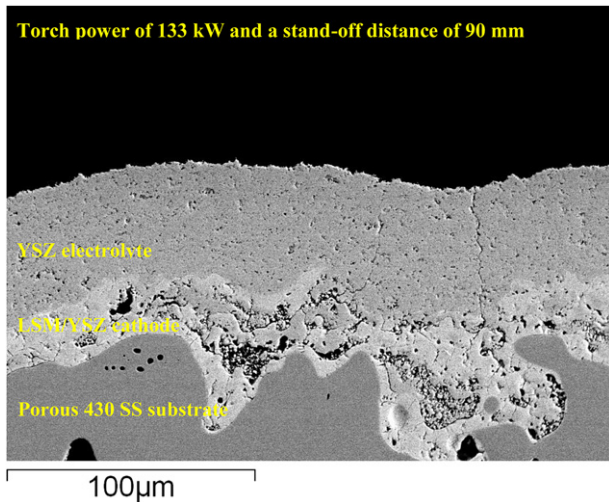


Fig. 1. An SEM image of a cross-section of a sample SOFC half-cell, in which the YSZ electrolyte was deposited on the LSM/YSZ + MG 2 substrate using the G2 spray condition.

distance of 90 mm, on the LSM/YSZ + MG 2 substrate were also measured at elevated temperatures up to 750 °C.

Among the various methods available for residual stress measurement, XRD is a powerful method due to its non-destructive nature. It can also be used to distinguish stresses in different phases. The residual stresses in the electrolytes were determined as a function of temperature using a high-temperature X-ray diffractometer. In measuring the residual stress using XRD, the strain in the crystal lattice is determined from the change in interplanar spacing. The associated residual stress is determined using the elastic constant of the coating material, assuming a linear elastic distortion of the crystal lattice planes.

Fig. 2 shows a sample coordinate system used for the strain determination. σ_1 , σ_2 , and σ_3 are the principal stresses acting in the principal directions, ϕ is the rotation angle around the sample normal, ψ is the angle between the sample normal and the normal of the diffracting plane, $\varepsilon_{\phi\psi}$ is the strain in the direction of measurement defined by the angles ϕ and ψ , and σ_ϕ is the single stress acting in a chosen direction, i.e., at an angle ϕ to σ_1 . It was assumed that $\sigma_3 = 0$ because the measurement was made near the surface of the thin coating. The commonly used $\sin^2\psi$ method has been adopted for the residual stress measurement in the present study. Details of the $\sin^2\psi$ method have been described elsewhere

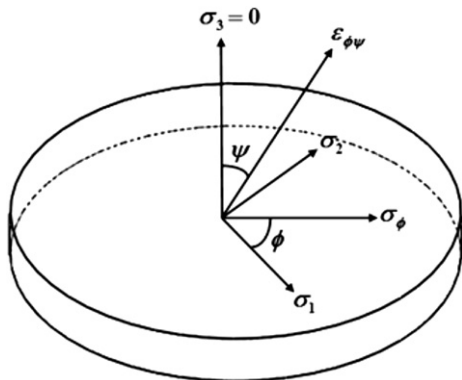


Fig. 2. Schematic diagram showing the coordinate system used to determine the strain using XRD.

[24,25]. The configuration for the diffraction measurement and stress analysis is schematically shown in Fig. 3, where the three sample rotation angles ω , ϕ and ψ are indicated. The measurement of residual stresses with the $\sin^2\psi$ method requires at least ψ tilt [26]. This ψ tilt can be achieved by ω -rotation (iso-inclination) or ψ -rotation (side-inclination), as shown in Fig. 3. In this study, the side-inclination method (ψ -method) was used. In this case, the sample normal (S_3) is out of the diffractometer plane (a plane containing the X-ray incident beam and diffracted beam) for all non-zero ψ tilt angles.

The residual stress analysis was performed using a Panalytical X'Pert PRO MRD (Panalytical B.V., Almelo, Netherlands) high-resolution X-ray diffractometer, which is equipped with a high temperature stage reaching up to 1100 °C in conjunction with a vacuum system using Cu-K α radiation. An initial scan was performed with the diffraction angle 2θ ranging from 10 to 150° to identify the diffraction peaks. A diffraction peak having a 2θ angle greater than 120° is usually recommended for residual stress evaluation due to its greater sensitivity to variation in the d -values according to Bragg's law [27], where d is the interplanar spacing. Therefore, a diffraction peak at $2\theta=125.2^\circ$ was selected for the residual stress determination based on the pre-scan diffraction pattern of the coating. The XRD spectra surrounding this peak were scanned from $\psi = -40^\circ$ to $\psi = +40^\circ$ in 9 steps at each temperature. For the coatings tested at elevated temperatures, the sample stage was heated from room temperature to 750 °C in steps of 250 °C. At each temperature, the sample was held a minimum of 15 min prior to measurement to allow the sample to reach thermal equilibrium. X'pert Data Collector software (Panalytical B.V.) was used to coordinate the movements of the X-ray source, detector, and sample stage, and to automate the measurement and data collection processes. The analysis of the measured data was performed using X'pert Stress software (Panalytical B.V.). The peak profile was evaluated using the constant + range background correction method and fitted with a parabolic function to identify the center position of the peak [28].

It should be noted that coating roughness must be considered when evaluating residual stress by XRD methods. For roughness to be insignificant, the average roughness (R_a) should be small in comparison to the mean X-ray penetration depth ($\tau_{0.3}$) at a tilt angle corresponding to $\sin^2\psi = 0.3$ [28]. Otherwise, stress relaxation in surface asperities can contribute to a lower value of measured residual stress. However, surface modification techniques that decrease roughness, such as grinding and polishing,

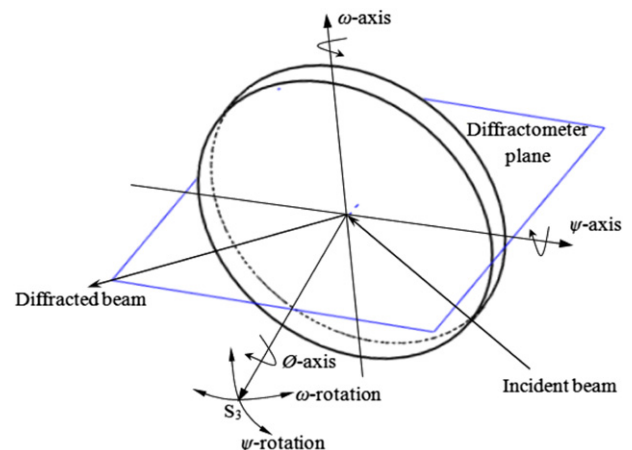


Fig. 3. Schematic view showing ψ tilt by iso-inclination (ω -rotation) or side-inclination (ψ -rotation).

should be avoided because they can alter the stress state to a significant extent. The mean X-ray penetration can be calculated using the following equation [26],

$$\tau_{0.3} = \frac{\sin \theta \cos \psi \ln(1 - G_T)}{2\mu}, \quad (1)$$

where $\tau_{0.3}$ is the mean penetration depth, μ is the linear absorption coefficient, and G_T is the fraction of the total diffraction intensity contributed by the surface layer of thickness T . A G_T value of 0.99 was previously calculated using Bragg–Brentano geometry for an electrolyte with thickness of 45 μm [29]. In the present study, the calculated mean X-ray penetration depth was 27 μm , based on a wavelength of $\lambda = 1.5406 \text{ \AA}$ and a bulk density of 5.96 g cm^{-3} of YSZ [30], which is higher than the measured R_a of approximately 8 μm for electrolytes on the LSM/YSZ + MG 2 substrates. The electrolytes on the MG 0.2 substrates had even lower roughness. Therefore, the effect of coating roughness on the residual stress was not considered.

2.3. Microstructural analysis

To examine coating microstructures, the samples were mounted in epoxy, sectioned using a diamond saw, re-mounted in epoxy, and then polished using standard metallographic methods. The polished samples were examined with a scanning electron microscope (SEM) (JSM-6380LV, JEOL Co. Ltd., Akishima, Japan). The thicknesses of the electrolyte layers were calculated from the coating weights and adjusted by multiplying by a thickness-to-weight gain ratio determined from image analysis of selected coatings.

3. Results and discussion

3.1. X-ray diffraction and $\sin^2\psi$ measurements

Fig. 4 shows a typical XRD pattern from an initial scan over the electrolyte on the LSM/YSZ + MG 2 substrate at room temperature. The arrow indicates the (531) diffraction peak positioned at a 2θ angle of 125.2° that was selected for the residual stress measurements. All the peaks in the diffraction pattern correspond to those of cubic YSZ, and there are no peaks from LSM in the cathode layer or from stainless steel in the porous metal support (Fig. 1). The phase diagram of 8 mol% YSZ indicates that this cubic structure remains stable at SOFC operating temperatures of $650\text{--}800^\circ\text{C}$ [31].

Fig. 5 shows the change of the diffraction peak of the selected (531) plane with the tilt of ψ . The (531) peak position shifts to lower

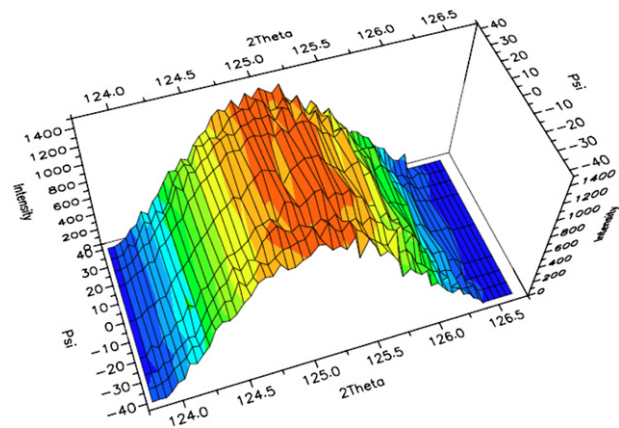


Fig. 5. XRD patterns of the (531) plane diffraction peak of a sample YSZ electrolyte fabricated on the LSM/YSZ + MG 2 substrate using the G2 spray condition with changing ψ at room temperature.

angles with increasing ψ , indicating that the interplanar spacing (d) increases. This behavior suggests that the residual stress in the surface layer is tensile in nature. Fig. 6 shows a typical $\epsilon - \sin^2\psi$ diagram for the (531) diffraction plane of the electrolyte on the LSM/YSZ + MG 2 substrate at room temperature. The diamonds indicate negative ψ tilt and the triangles indicate positive and zero ψ tilt. The solid line represents the linear least-squares fitting to both sets of data points. Although the data are slightly scattered, the lattice strain ϵ increases approximately linearly with increasing $\sin^2\psi$. Residual stress can therefore be estimated from the slope of the $\epsilon - \sin^2\psi$ best fitting line. In the stress measurement by XRD, the stress in the YSZ layer can be estimated using the diffraction from a specified diffracting plane ((531) in this study) of crystallites that are oriented in the specified direction. Therefore, the elastic constant and Young's modulus (E) and Poisson's ratio (ν) are different from those measured by mechanical methods, and these elastic constants should be measured by the XRD method [32]. However, there are no data available in the open literature for X-ray elastic constants measured by the XRD method for the YSZ (531) plane. Sattonnay *et al.* [33] derived the room temperature elastic constants $E_{(531)}$ and $\nu_{(531)}$ of YSZ using the Hill–Neerfeld model [34] and using reported single crystal elastic constants for cubic YSZ [35]. Normally the Hill–Neerfeld model best matches the experimentally determined elastic constant; therefore, these values were used in the present analysis. Since $E_{(531)}$ at elevated temperatures

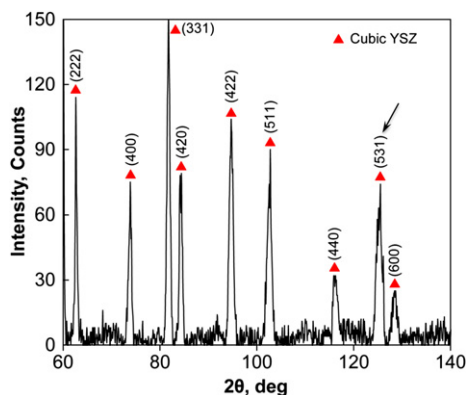


Fig. 4. X-ray diffraction pattern for a sample YSZ electrolyte at room temperature fabricated on the LSM/YSZ + MG 2 substrate using the G2 spray condition.

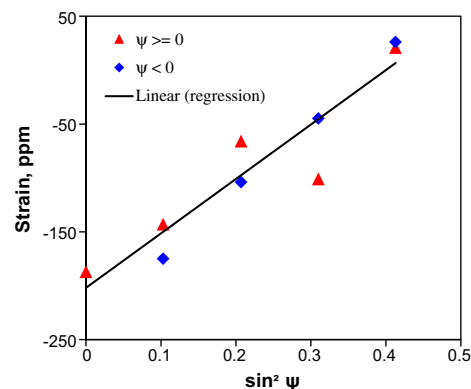


Fig. 6. Typical $\epsilon - \sin^2\psi$ diagram for the (531) diffraction plane of the YSZ electrolyte determined at room temperature, where the solid line represents the linear least squares fitting.

was not available, it was assumed that the temperature-dependent behavior of $E_{(531)}$ follows the same trend as that of the bulk E as a function of temperature, as determined by Huang and Harter [23] via a linear least squares fitting. The $E_{(531)}$ and $\nu_{(531)}$ values used in this study are given in Table 2.

3.2. Influence of torch power and stand-off distance on residual stress

Residual stresses in plasma sprayed coatings are known to vary significantly with deposition conditions. Torch power and stand-off distance are two key factors in controlling the performance and stress state of coatings. Therefore, the residual stresses were evaluated with the various torch powers and stand-off distances listed in Table 1. Furthermore, it has been shown that electrolyte coating properties are strongly dependent on the substrate [36], so both the LSM/YSZ + MG 2 and the MG 0.2 substrates were used for these tests.

Fig. 7 shows the room temperature electrolyte residual stress as a function of torch power at a constant stand-off distance of 90 mm, using coating deposition conditions of G2, G4, and G5 (Table 1). Fig. 8 shows the relationship between room temperature electrolyte residual stress and stand-off distance with a constant torch power of 133 kW, using coating conditions G1, G2, and G3 (Table 1). The magnitude of room temperature residual stresses in the electrolytes ranged from 35 to 91 MPa on both substrates with the various torch power and stand-off distance combinations (Table 1). As previously mentioned, quenching stress is always tensile, while thermal mismatch stress can be tensile or compressive. In the present case, the thermal mismatch stress in the YSZ layer is compressive because the CTE of YSZ (10.5 ppm K^{-1}) is lower than that of both the LSM/YSZ cathode (11.7 ppm K^{-1}) and the 430 stainless steel substrate (11.4 ppm K^{-1}) [37–39]. The tensile nature of the residual stress indicates that the quenching stress component is larger than the thermal mismatch stress component. This result is likely partially due to the fairly small differences between the CTEs of the three cell layers.

The magnitude of residual stress depends in part on the microstructural attributes of the coating. Fig. 9 shows sample SEM images of the G2 electrolytes prior to and after high temperature XRD measurement (the results from high temperature XRD measurements are discussed in Section 3.3). Three categories of microstructural defects are present in the electrolyte: microcracks, small pores, and vertical or segmentation cracks, as indicated by arrows in Fig. 9. The extent to which all three defect types occur can be reduced, though not always independently of each other, by modifying SPS processing parameters. Microcracks are generated primarily during quenching of the molten splats to relieve the tensile stresses. The small pores are formed by a number of mechanisms, including incomplete penetration of molten splats into surface crevices and the inclusion of partially melted particles in the coating [17,40]. The segmentation cracks run through most or all of the coating thickness, and they also form to relieve tensile stress. Many previous studies have identified segmentation cracks in suspension plasma sprayed coatings [18,41–43]. The microcracks and small pores relax stress locally, while the segmentation cracks provide stress relief for larger sections of the coating.

Table 2
High temperature E and ν values used in this study for the (531) plane.

Temperature, °C	ν	E , GPa
RT	0.35 [33]	242 [33]
250	0.35	218
500	0.35	195
750	0.35	173

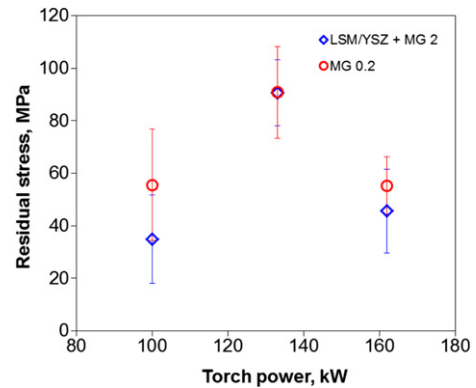


Fig. 7. Room temperature electrolyte residual stress as a function of torch power at a constant stand-off distance of 90 mm.

The residual stress was highest in the electrolytes produced with a torch power of 133 kW compared to those produced at 100 kW and 162 kW, on both substrates (Fig. 7). These results are partly attributed to microstructural changes arising with varying torch power. Figs. 10 and 11 show sample SEM micrographs of electrolytes on the MG 0.2 and the LSM/YSZ + MG 2 substrates, respectively. Electrolyte porosity decreases with increasing torch power, as the 100 kW coatings (Figs. 10a and 11a) appear more porous than the 133 kW (Figs. 10b and 11b) and 162 kW (Figs. 10e and 11e) coatings. With lower torch powers, the plasma enthalpy may not have been adequate to completely melt all powder particles, or molten droplets may have resolidified prior to impact. These pores relieve stress, and therefore the 100 kW coatings showed lower levels of residual stress compared to the higher torch power coatings. As torch power is increased, denser coatings with improved inter-splat adhesion are produced, and there is also higher heat flux from the plasma to the coating and substrate during deposition. Such factors have previously been shown to promote the formation of segmentation cracks in SPS coatings [36,41,43]. These segmentation cracks provide stress relief in the coatings, resulting in residual stresses levels in the electrolytes that are smaller than the tensile fracture strength of $\sim 200 \text{ MPa}$ or bending fracture strength of $\sim 350 \text{ MPa}$ of free standing 8 mol% YSZ [44]. On the MG 0.2 substrates, no segmentation cracks were observed in the coatings fabricated at 100 and 133 kW plasma powers, but segmentation cracks are visible in the coatings made at 162 kW plasma power. Accordingly, on the MG 0.2 substrates, the 133 kW electrolytes have the highest residual stress because

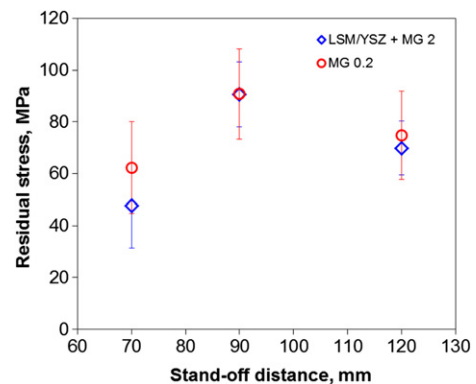


Fig. 8. Room temperature electrolyte residual stress as a function of stand-off distance during fabrication with a constant torch power of 133 kW.

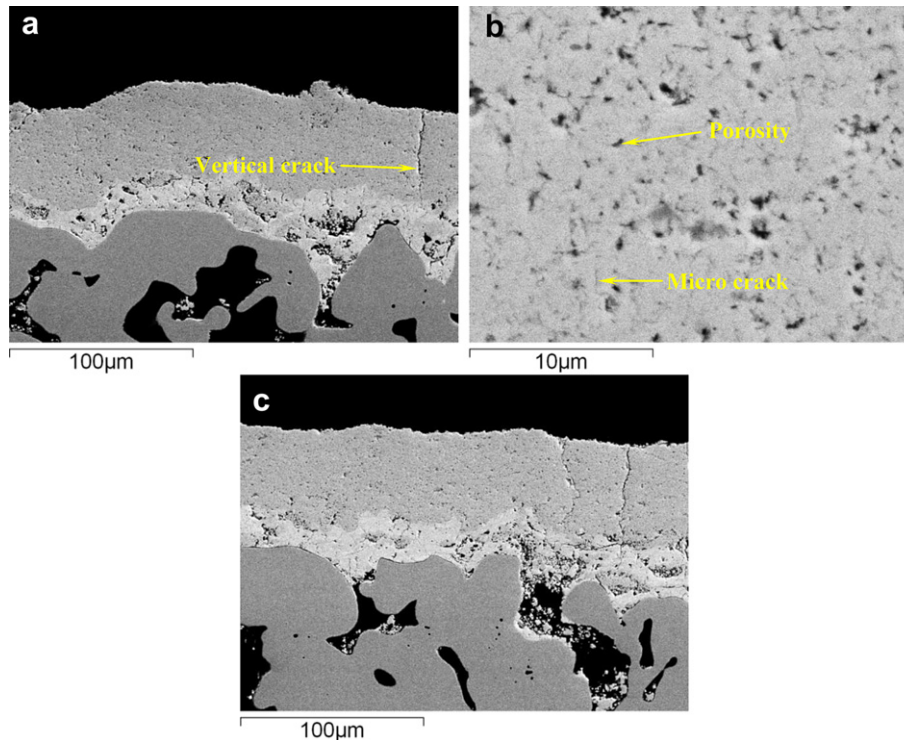


Fig. 9. Sample SEM images of G2 electrolytes on the LSM/YSZ + MG 2 substrates: (a) and (b) before and (c) after high-temperature XRD measurement.

they are denser than the 100 kW coatings and have fewer segmentation cracks than the 162 kW coatings. On the LSM/YSZ + MG 2 substrates, segmentation cracks are visible in all of the coatings examined, although the frequency and severity of these cracks increases with torch power, as is visible in Fig. 11 and has been previously reported with these spray conditions [36]. Therefore, on the LSM/YSZ + MG 2 substrates, it is believed that the more severe and frequent segmentation cracks in the 162 kW coating are the reason for its lower residual stress compared to the 133 kW coating.

With both substrates, residual stress was highest in electrolytes made at a stand-off distance of 90 mm compared with the 70 mm and 120 mm electrolytes (Fig. 8). Reducing the stand-off distance had a similar effect as increasing the torch power on both residual stress and microstructure. Shorter spray distances resulted in denser coatings with more severe segmentation cracking (Figs. 10d and 11d) compared to longer spray distances, and similar microstructural trends have been previously reported for these spray conditions [36]. Increasing the spray distance had a similar effect as reducing the torch power. Longer spray distances produce coatings with more porosity (Figs. 10c and 11c) because the molten droplets are cooler (or resolidified) and have less momentum at impact. Bacciochini *et al.* [45] have also reported that longer stand-off distances lead to coatings with more porosity and reduced inter-splat adhesion. From the above analysis and the observed results, it can be concluded that the dependence of residual stresses on the torch power and stand-off distance is similar, but in a reverse order (i.e., a higher torch power has a similar effect as a shorter stand-off distance, and vice versa).

The electrolytes on the LSM/YSZ + MG 2 and the MG 0.2 substrates show similar residual stress trends with varying torch power and stand-off distance. However, the coatings on MG 0.2 substrates showed comparatively higher residual stress with all spray conditions except the 133 kW torch power and 90 mm stand-off distance condition. The coatings on the MG 0.2 substrates had

less frequent and less severe segmentation cracking compared to those on the LSM/YSZ + MG 2 substrates, which may be partially responsible for the higher residual stresses in the MG 0.2 coatings. In the shortest stand-off distance (Fig. 10d) and highest torch power (Fig. 10e) electrolytes on MG 0.2 substrates, the vertical cracks generally did not penetrate through the entire coating thickness. In contrast, the vertical cracks in the comparable coatings on the LSM/YSZ + MG 2 substrates (Fig. 11e and d) penetrated through the entire electrolyte thickness and occasionally into the cathode layer. Furthermore, the electrolytes on the MG 0.2 substrates are less porous than those on the relatively rougher LSM/YSZ + MG 2 substrates because the surface asperities increase porosity [36]. As pores provide stress relief, the lower porosity of the electrolytes on the MG 0.2 substrates may also be partially responsible for their higher residual stress compared to those on the LSM/YSZ + MG 2 substrates. These results indicate that coating microstructure and residual stress are affected by the substrate characteristics as well as by the process conditions.

3.3. Temperature-dependent residual stress

Fig. 12 shows the residual stress as a function of temperature of the G2 electrolyte on the LSM/YSZ + MG 2 substrates (Table 1). At room temperature, the residual stress was tensile, with a value of approximately 90 MPa. The tensile residual stress decreased with increasing temperature. At a typical SOFC operating temperature of 750 °C, the residual stress of the electrolyte was approximately 39 MPa.

Several mechanisms may be associated with the observed changes in residual stresses at elevated temperatures shown in Fig. 12. These factors include changes in the Young's modulus of the electrolyte material, the potential formation of microcracks, and changes in thermal expansion mismatch between layers. First, the Young's modulus of YSZ decreases with increasing temperature, as shown in Table 2. This decrease would therefore reduce its residual

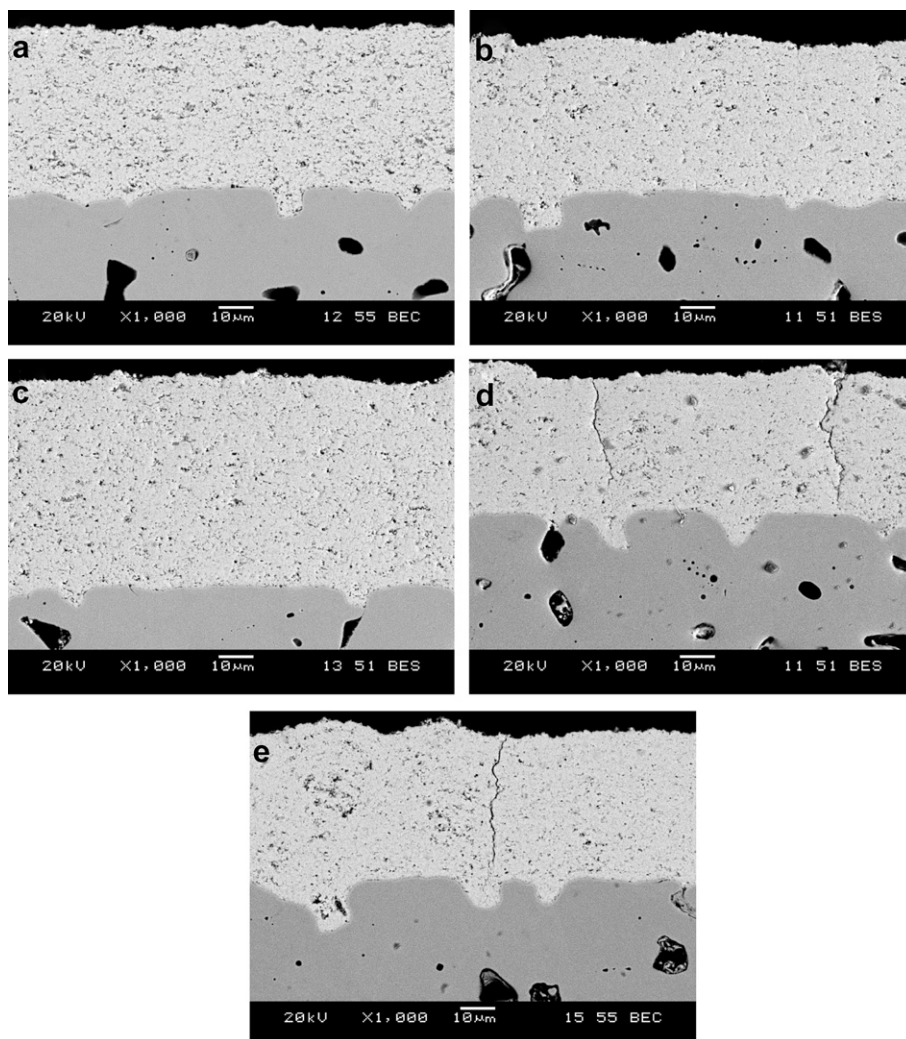


Fig. 10. SEM cross-section images of electrolytes on MG 0.2 substrates with spray conditions: (a) 100 kW, 90 mm, (b) 133 kW, 90 mm, (c) 133 kW, 120 mm, (d) 133 kW, 70 mm, and (e) 162 kW, 90 mm.

stress with increasing temperature. Second, it is possible that the increase in temperature may have resulted in the formation of additional microcracks. Teixeira *et al.* [46] reported that stress relief at elevated temperature in zirconia TBC coatings can occur by microcrack formation. However, it is difficult to determine whether additional microcracks formed in the present study, as the microstructures looked similar in coatings examined both before and after the high-temperature stress determination. Third, increasing the temperature from room temperature to 750 °C would change the thermal expansion mismatch between the electrolyte, cathode and stainless steel support. Church *et al.* [47] showed that the CTEs of both 430 stainless steel and YSZ increase with temperature. However, the CTE of the steel exhibits a steeper increase than that of YSZ, which would increase tensile stress in the electrolyte during heating.

Another potential stress relief mechanism at higher temperatures is the occurrence of creep deformation of the porous stainless steel support. Creep becomes relevant in materials at temperatures near half of their melting point (in Kelvin) [10]. The melting of 430 stainless steel is reported to begin at 1427 °C [48]. Creep may therefore be expected to occur when the test temperature is above ~600 °C. Indeed, as pointed out by Liu *et al.* [10] the potential creep deformation of the SOFC support structure should not be

neglected at typical cell operating temperatures of 650–800 °C. While the creep behavior of 430 stainless steel is not available in the open literature [10], creeping of steel supports could have contributed to the reduction in residual stress in the electrolyte layer at 750 °C. However, creep is a time-dependent phenomenon, and in the present study, the samples were only held at 750 °C for approximately 2 h. Further analysis would be required in order to identify the potential contribution of creep toward the decrease in residual stress at this temperature. Considering all factors, the decrease of the residual stress with increasing temperature (Fig. 12) is a consequence of the combined changes in the Young's modulus and thermal expansion mismatch, and may have also been partially due to formation of microcracks in the electrolyte and creep deformation in the porous stainless steel substrate.

These electrolyte coatings are still under development to improve their suitability for SOFCs. By a combination of measures, it is hoped to further improve coating density while at the same time reducing or eliminating segmentation cracking. It is known that electrolytes made by plasma spraying do not yet perform as well as those made by conventional wet ceramic methods. Nonetheless, plasma spraying is a promising fabrication method for SOFCs because it permits direct deposition of the functional layers on metal supports and may offer cost advantages over conventional

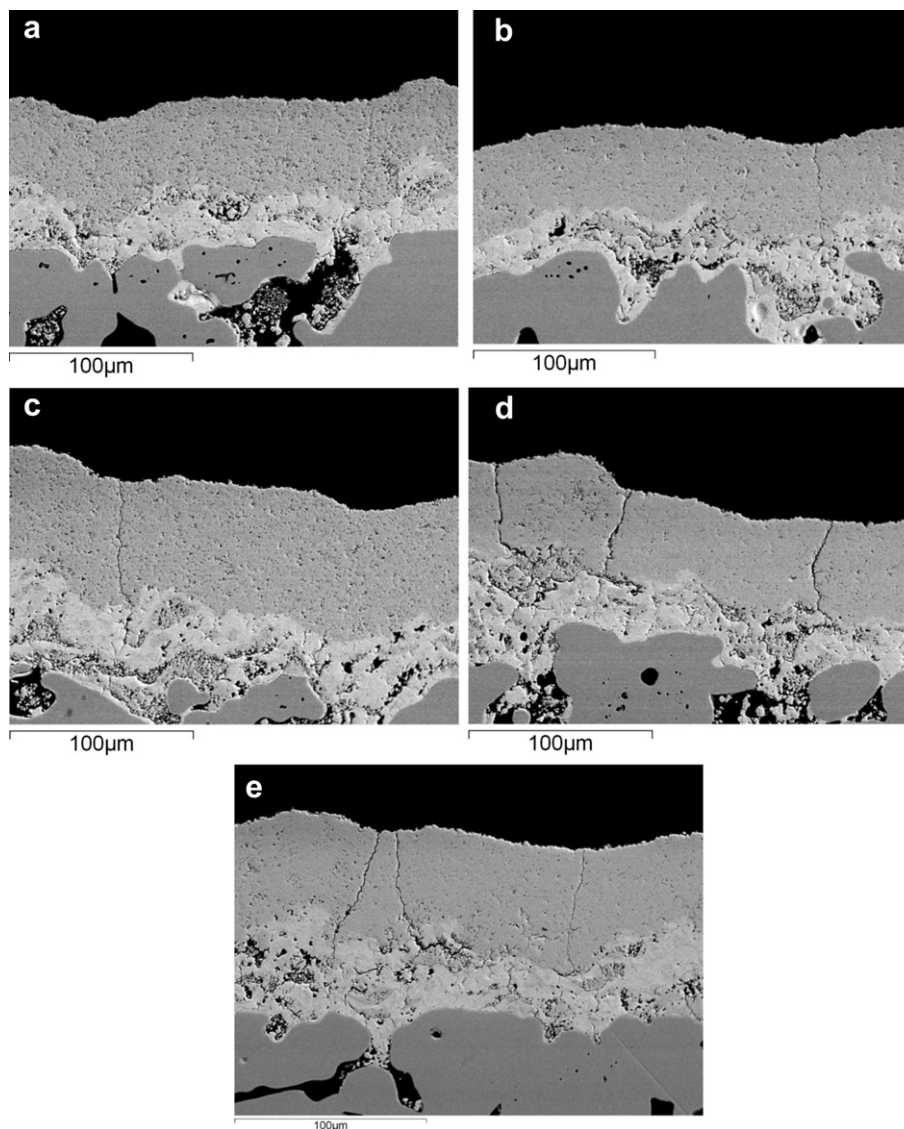


Fig. 11. SEM cross-section images of electrolytes on the LSM/YSZ + MG 2 substrate, (a) 100 kW, 90 mm, (b) 133 kW, 90 mm, (c) 133 kW, 120 mm, (d) 133 kW, 70 mm, and (e) 162 kW, 90 mm.

fabrication methods. The results of the present study aid this development process with useful information for further understanding mechanical properties such as flexural strength, fracture toughness and adhesion strength.

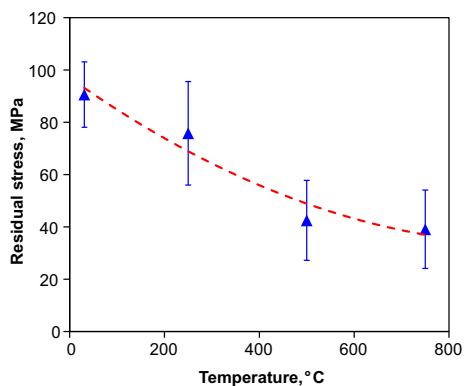


Fig. 12. Temperature dependent residual stress in the G2 electrolytes on the LSM/YSZ + MG 2 substrates.

4. Conclusions

Residual stresses at room and elevated temperatures were evaluated in SOFC electrolyte coatings made by SPS on two different substrates using a variety of processing conditions. At room temperature, residual stresses were tensile and ranged from 35 to 91 MPa, depending on which processing conditions and substrate were used. Of the deposition conditions studied, the coating made with the intermediate torch power of 133 kW and intermediate stand-off distance of 90 mm exhibited the highest residual stress. This coating had a relatively dense microstructure with relatively small amount of vertical cracking. With lower torch powers and longer stand-off distances, the resulting electrolytes were more porous, while with higher torch powers and shorter stand-off distances, the electrolytes had more severe vertical cracking. In the electrolyte made with a torch power of 133 kW and a stand-off distance of 90 mm, residual stress decreased to approximately 39 MPa when the temperature was increased step-wise from room temperature to 750 °C. The decrease of residual stress with increasing temperature is associated with several factors, including changes in Young's modulus and thermal

expansion mismatch, and also potentially the formation of micro-cracks and possible creep of the porous stainless steel substrate.

Acknowledgments

The authors would like to thank the Natural Sciences and Engineering Research Council of Canada (NSERC), Premier's Research Excellence Award (PREA), NSERC-Discovery Accelerator Supplement (DAS) Award, AUTO21 Network of Centers of Excellence, and Ryerson Research Chair (RRC) program for providing financial support. The assistance of Q. Li, A. Machin, J. Amankrah, and R. Churaman (Ryerson University) and T. Li (Centre for Advanced Coating Technologies, University of Toronto) in performing the experiments is gratefully acknowledged.

References

- [1] J. Murray, D. King, *Nature* 481 (2012) 433–435.
- [2] D.A. Howey, *Nat. Clim. Change* 2 (2012) 28–29.
- [3] T. Suzuki, Z. Hasan, Y. Funahashi, T. Yamaguchi, Y. Fujishiro, M. Awano, *Science* 325 (2009) 852–855.
- [4] Y.H. Huang, R.I. Dass, Z.L. Xing, J.B. Goodenough, *Science* 312 (2006) 254–257.
- [5] Z.L. Zhan, S.A. Barnett, *Science* 308 (2005) 844–847.
- [6] C.K. Dyer, *J. Power Sources* 106 (2002) 31–34.
- [7] E.D. Wachsman, K.T. Lee, *Science* 334 (2011) 935–939.
- [8] Z. Shao, S.M. Haile, *Nature* 431 (2004) 170–173.
- [9] L. Rose, O. Kesler, C. Decès-Petit, T. Troczynski, R. Maric, *Int. J. Green Energy* 6 (2009) 638–645.
- [10] W.N. Liu, X. Sun, M.A. Khaleel, *Fuel Cells* 10 (2010) 703–717.
- [11] P. Lamp, J. Tachtler, O. Finkenwirth, S. Mukerjee, S. Shaffer, *Fuel Cells* 3 (2003) 1–7.
- [12] D. Waldbillig, O. Kesler, *J. Power Sources* 191 (2009) 320–329.
- [13] M. Brandner, M. Bram, J. Froitzheim, H.P. Buchkremer, D. Stöver, *Solid State Ionics* 179 (2008) 1501–1504.
- [14] R. Hui, J. Berghaus, C. Decès-Petit, W. Qu, S. Yick, J. Legoux, C. Moreau, *J. Power Sources* 191 (2009) 371–376.
- [15] Q. Huang, J. Berghaus, D. Yang, S. Yick, Z. Wang, B. Wang, R. Hui, *J. Power Sources* 177 (2008) 339–347.
- [16] J. Matejcek, S. Sampath, P.C. Brand, H.J. Prask, *Acta Mater.* 47 (1999) 607–617.
- [17] R. McPherson, *Surf. Coat. Technol.* 39–40 (1989) 173–181.
- [18] D. Waldbillig, O. Kesler, *Surf. Coat. Technol.* 205 (2011) 5483–5492.
- [19] Y. Wang, J.G. Legoux, R. Neagu, S. Hui, B.R. Marple, *J. Therm. Spray Technol.* 21 (2012) 7–15.
- [20] O. Kesler, J. Matejcek, S. Sampath, S. Suresh, T. Gnaeupel-Herold, P.C. Brand, H.J. Prask, *Mater. Sci. Eng. A* 257 (1998) 215–224.
- [21] W. Fischer, J. Malzbender, G. Blass, R.W. Steinbrech, *J. Power Sources* 150 (2005) 73–77.
- [22] J. Malzbender, W. Fischer, R.W. Steinbrech, *J. Power Sources* 182 (2008) 594–598.
- [23] K. Huang, H.D. Harter, *Solid State Ionics* 181 (2010) 943–946.
- [24] H. Yakabe, Y. Baba, T. Sakurai, Y. Yoshitaka, *J. Power Sources* 135 (2004) 9–16.
- [25] I.C. Noyan, J.B. Cohe, *Mater. Sci. Eng.* 75 (1985) 179–193.
- [26] B.B. He, *Two Dimensional X-Ray Diffraction*, vol. 19, John Wiley & Sons, Inc., 2009.
- [27] P.S. Prevèy, *Metals Handbook*, vol. 10, ASM, Metals Park, 1986, pp. 380–392.
- [28] W. Fischer, H. Gruhn, W. Mallèner, *Mater. Sci. Forum* 228–231 (1996) 481–486.
- [29] K. Ozalas, B.F. Hajek, *Clay Clay Miner.* 44 (6) (1996) 811–817.
- [30] I.R. Gibson, G.P. Dransfield, J.T.S. Irvine, *J. Mater. Sci.* 33 (1998) 4297.
- [31] J. Ilavsky, J.K. Stalick, *Surf. Coat. Technol.* 127 (2000) 120–129.
- [32] H. Yakabe, Y. Baba, T. Sakurai, M. Satoh, I. Hirose, Y. Yoda, *J. Power Sources* 131 (2004) 278–284.
- [33] G. Sattonnay, M. Lahrachi, M. Herbst-Ghysel, F. Garrido, L. Thomè, *J. Appl. Phys.* 101 (2007) 103516.
- [34] R. Hill, *Proc. Phys. Soc.* 65 (1952) 349–354.
- [35] R.P. Ingel, D. Lewis III, *J. Am. Ceram. Soc.* 71 (4) (1988) 265–271.
- [36] M. Marr, O. Kesler, *J. Therm. Spray Technol.*, under review.
- [37] S. Molin, B. Kusz, M. Gazda, P. Jasinski, *J. Power Sources* 181 (2008) 31–37.
- [38] A. Atkinson, B. Sun, *Mater. Sci. Technol.* 23 (2007) 1137–1143.
- [39] D. Cui, M. Cheng, *J. Power Sources* 192 (2009) 400–407.
- [40] X.C. Zhang, B.S. Xu, F.Z. Xuan, S.T. Tu, H.D. Wang, Y.X. Wu, *Appl. Surf. Sci.* 255 (2009) 4362–4371.
- [41] S. Kozerski, L. Latka, L. Pawlowski, F. Cernuschi, F. Petit, C. Pierlot, H. Podlesak, J.P. Laval, *J. Eur. Ceram. Soc.* 31 (12) (2011) 2089–2098.
- [42] R. Vaßen, H. Kaßner, G. Mauer, D. Stöver, in: *Proc. of the International Thermal Spray Conference*, ASM International, May 4–7, 2009 (Las Vegas, NV), pp. 162–167.
- [43] H. Kassner, R. Siegert, D. Hathiramani, R. Vassen, D. Stöver, *J. Therm. Spray Technol.* 17 (1) (2008) 115–123.
- [44] J. Kondoh, H. Shiota, K. Kawachi, T. Nakatani, *J. Alloys Compd.* 365 (2004) 253–258.
- [45] A. Bacciochini, J. Ilavsky, G. Montavon, A. Denoirjean, F. Ben-ettouil, S. Valette, P. Fauchais, K. Wittmann-tenezec, *Mater. Sci. Eng. A* 528 (2010) 91–102.
- [46] V. Teixeira, M. Andritschky, W. Fischer, H.P. Buchkremer, D. Stöver, *Surf. Coat. Technol.* 120–121 (1999) 103–111.
- [47] B.C. Church, T.H. Sanders, R.F. Speyer, J.K. Cochran, *Mater. Sci. Eng. A* 452–453 (2007) 334–340.
- [48] E. Klar, P. Samal, *Powder Metallurgy Stainless Steels*, ASM International, 2007.